Influence of almond's canopy-induced shadows on actual evapotranspiration estimation by the TSEB model using sUAS multispectral and thermal imagery

Moises Rodrigo Duran-Gomez
m.duran-gomez@usu.edu
Utah State University
Alfonso Torres-Rua
Utah State University
Lawrence Hipps
Utah State University
William Kustas
Agricultural Research Service
Nicolas E. Bambach
University of California, Davis
Kyle Knipper
Agricultural Research Service
Ian Robb Wright
University of California, Davis
Andrew J. McElrone
University of California, Davis
John H. Prueger
Agricultural Research Service
Joe G. Alfieri
Agricultural Research Service
Calvin Coopmans
Utah State University
Karem Meza
University of California, Davis
Ian Gowing
Utah State University
Mallika Nocco
University of Wisconsin–Madison

Sebastian J Castro
University of California, Davis
Andrew J. Gal
University of California, Davis
Peter Tolentino
Agricultural Research Service

Research Article

Keywords: TSEB, almonds, sUAS, canopy-induced shadows, LAI

Posted Date: August 13th, 2025

DOI: https://doi.org/10.21203/rs.3.rs-7306171/v1

Additional Declarations: No competing interests reported.

Version of Record: A version of this preprint was published at Irrigation Science on February 28th, 2026. See the published version at https://doi.org/10.1007/s00271-026-01092-7.

Influence of almond's canopy-induced shadows on actual evapotranspiration estimation by the TSEB model using sUAS multispectral and thermal imagery

M. R. Duran-Gomez[1]*, A. Torres-Rua1, L. Hipps[2], W. Kustas[3], N. E. Bambach[4], K. Knipper[5], I. Wright[6], A. J. McElrone[4,7], J. H. Prueger[8], J. G. Alfieri[3], C. Coopmans[9], K. Meza[4], I. Gowing[10], M. Nocco[11], S. J. Castro[4], A. Gal[4], P. Tolentino[5]

[1]*Civil and Environmental Engineering Department, Utah State University, Old Main Hill, Logan, UT 84322, USA.

[2]Plants, Soils, and Climate Department, Utah State University, Old Main Hill, Logan, UT 84322, USA.

[3]Agricultural Research Service, Hydrology and Remote Sensing Laboratory, US Department of Agriculture, Beltsville, MD 20705, USA.

[4]Department of Land, Air, and Water Resources, University of California – Davis, Davis, CA 95616, USA.

[5]Sustainable Agricultural Water Systems Research Unit, ARS, USDA, Davis, California

[6]Agricultural & Environmental Sciences, University of California – Davis, Davis, CA 95616, USA.

[7]Agricultural Research Service, USDA, Davis, CA 95616, USA.

[8]National Laboratory for Agriculture and the Environment, Agricultural Research Service, US Department of Agriculture, Ames, IA 50011, USA.

[9]Electrical & Computer Engineering Department, Utah State University, Old Main Hill, Logan, UT 84322, USA

[10]Utah Water Research Laboratory, Utah State University, Logan, UT 84322, USA.

[11]Biological Systems Engineering Department, University of Wisconsin–Madison, Madison, WI 53706, USA.

*Corresponding author(s). E-mail(s): m.duran-gomez@usu.edu

Abstract

Over the past decade, the estimation of water requirements in almond orchards has improved through the application of remote sensing models like the Two-Source Energy Balance (TSEB) model using various remote sensing platforms. However, there is limited understanding of how canopy-induced shadows influence surface reflectance and thermal infrared (TIR) signals particularly from small Unmanned Aircraft System (sUAS) imagery in energy balance models, and the effect on Latent Heat Flux (LE) estimations. This study evaluates LE estimates from the Priestley-Taylor TSEB model (TSEB-PT) with and without shadow filtering using sUAS-based multispectral and TIR imagery. It establishes a baseline for the impact of shadow exclusion on model inputs and performance. Datasets were collected in 2021 and 2022, as part of the USDA led Tree-crop Remote sensing of Evapotranspiration eXperiment (T-REX) in almonds orchards across California. LAI-2200C Plant Canopy Analyzer measurements facilitated the calibration of an empirical Leaf Area Index (LAI) model based on canopy fractional cover (FC) and NDVI (R^2 = 0.68). Shadow filtering caused land surface temperature (LST) differences up to 5°C in young to semi-mature orchards (FC 0.40-0.80). In contrast, mature orchards (FC > 0.80) showed minimal influence due to the limited shadow occurrence on the imagery. Shadows appeared to reduce surface albedo (α_{alb}), mainly in interrow areas, thereby affecting the absorption of radiation and the partitioning of energy balance components. Their presence in sUAS imagery also hindered canopy delineation, impacting the accuracy of key TSEB inputs derived from canopy physical characteristics. Thus, the influence of shadow on TSEB estimated LE was more significant in lower fractional tree covers. While LE estimated by TSEB-PT without shadow filtering showed better agreement with observations, combining instantaneous TIR imagery with solar-noon shortwave data is recommended for accurate ETa assessment using sUAS datasets. These baseline results can be improved with more advanced formulations, supporting continued research on E/T partitioning and water stress in almond orchards under varying environmental conditions, particularly when there is advection of hot dry air.

Keywords

TSEB, almonds, sUAS, canopy-induced shadows, LAI

1 Introduction

California's Central Valley has been the largest producer of almonds in the United States and the world for about two decades (O'Neil et al., 2016; Padilla, 2024), playing a crucial role in the region's economy (Fulton et al., 2019; Marvinney et al., 2020). This region heavily relies on irrigation to satisfy water demands by almond orchards and sustain profitable crop yields (Jha et al., 2022). However, farmers in the semi-arid region of California face a threat to yield due to more frequent and severe variations in weather and climatic conditions (Paciolla et al., 2024), causing scenarios of water scarcity due to recurrent severe and extreme droughts (Gebremichael et al., 2021; Helalia et al., 2021; Xia et al., 2017). In these circumstances, automated pressurized irrigation systems, such as micro-sprinklers and drip irrigation, are commonly used in almond orchards for their high-water use efficiency and direct water application to the almond root zone (Drechsler et al., 2022).

Irrigation scheduling requires constant information about water requirements or actual evapotranspiration (ETa, how much water is evaporating from the soil [E], and how much is transpired by the plants [T]) (Bellvert et al., 2018; Drechsler & Kisekka, 2022). Therefore, accurate spatial estimates of ETa are essential for reliable and effective irrigation management and planning in almond orchards (Jofre-Čekalović et al., 2022; Meza et al., 2023). This is particularly true from June to mid-July to prevent stress (McCullough-Sanden et al., 2021), and post-harvest, from August through September, to ensure starch accumulation for the following season (Davidson et al., 2021).

ETa (mm) can be directly estimated from latent heat flux (LE, W m^{-2}) conversion, using the latent heat of vaporization (J Kg^{-1}). Energy balance components, net radiation (Rn), latent heat flux (LE), sensible heat flux (H), and ground heat flux (G), can be estimated from surface energy balance models such as TSEB (Norman et al., 1995), METRIC (Allen et al., 2007), and SEBAL (Bastiaanssen et al., 1998) by utilizing optical (short-wave) and thermal (long-wave) spatial information. Although satellite sources, such as OpenET (https://openetdata.org), provide reliable monthly ETa data throughout the almond growing season, short-term variability is difficult to capture (K. Knipper et al., 2024). Previous research has showcased the reliability of the TSEB model in estimating instantaneous ETa when utilizing data from sUAS (R. Gao et al., 2022; Meza et al., 2023; Nassar et al., 2020; Nieto et al., 2019). Additionally, sUAS technology together with a constellation of satellites, has proven viable for acquiring TSEB model inputs at vine (Sanchez et al., 2017) and tree scale in pistachio and walnut (Gonzalez-Dugo et al., 2020; K. Wang & Jin, 2024). The TSEB model (Norman et al., 1995) has been implemented and validated across various vegetation types, including almonds (Anderson et al., 2024; Burchard-Levine et al., 2025; K. R. Knipper et al., 2019; Kustas et al., 2018; Quintanilla-Albornoz et al., 2024). In commercial almond orchards, trees are typically not stressed being supplied with enough water during peak season (Drechsler & Kisekka, 2022; McCullough-Sanden et al., 2021). Therefore, transpiration can theoretically be predicted based on tree canopy available energy, as in the Priestley-Taylor (1972) formulation for canopy transpiration (TSEB-PT) (Agam et al., 2010; Priestley & Taylor, 1972). The Priestley-Taylor coefficient α_{PT} (~1.26) is an enhancement of the equilibrium evaporation formula for the available energy of the tree crop assuming transpiration under non-stressed conditions.

Canopy-induced shadows, particularly evident sUAS imagery (Aboutalebi et al., 2019; Lu et al., 2022; Rojo et al., 2023), have been linked to variability in land surface temperature (LST). While this effect has been documented, its implications for surface energy balance modeling remain underexplored (Aboutalebi et al., 2019; R. Gao et al., 2023; Lu et al., 2022; Tunca, 2024). Shadows reduce the albedo (α_{alb}) on the surface of the orchard, decreasing the absorbed incoming solar radiation, therefore, raise the spatial and temporal variability of surface temperature and surface energy fluxes (Aboutalebi et al., 2019; Lu et al., 2022; Rojo et al., 2023; S. Wu et al., 2022). Similarly, diurnal variations in environmental parameters such as air temperature, humidity, and wind speed, in combination with shadow presence, also influences surface energy balance dynamics throughout the day (Aboutalebi et al., 2019; Lu et al., 2022). Moreover, shadow occurrence depends on the tree size, tree orchard spacings, and the azimuth angle relative to the latitude and orchard row orientation (Rojo et al., 2023). Given the high resolution of sUAS imagery, canopy-induced shadows can be accurately identified and filtered, allowing their influence on ETa estimation to be evaluated using the TSEB model (Cheng et al., 2020; Guimarães et al., 2023; Sarron et al., 2018; Zhang et al., 2019).

Shadows influence key TSEB inputs at the tree scale (Aboutalebi et al., 2019; Lu et al., 2022; Rojo et al., 2023), driven by orchard row orientation and spacing configuration (Drechsler et al., 2022; Duncan et al., 2024). These inputs include canopy height (H_{tree}), width-to-height ratio (W/H_{tree}), canopy fractional cover (FC), leaf area index (LAI), and land surface temperature (LST). When using high-resolution sUAS imagery, estimates of these variables must accurately represent tree physical characteristics, necessitating data aggregation techniques (Bellvert et al., 2018; Gelybó et al., 2013; Nassar et al., 2020; Nieto et al., 2019; Volk et al., 2023). Therefore, determining an appropriate grid size that is required by TSEB radiation, surface temperature and turbulent flux exchange formulations of the soil-canopy system is critical (Nassar et al., 2020).

Describing the required TSEB inputs, H_{tree}, W/H_{tree}, and FC, are defined by canopy-geometry, and various methodologies have been developed to obtain them for tree crops, utilizing multispectral imagery and a digital surface model (DSM) (L. Gao et al., 2020; R. Gao et al., 2023).

Next, LAI, a physical factor defined as the one-sided leaf area per unit ground area (Comba et al., 2020; R. Gao et al., 2022), and can have significant variability in clumped canopies such as almond's orchards (Ali & Imran, 2020; Jia & Wang, 2021; Maldera et al., 2023). Direct and indirect field LAI measurements are often labor-intensive and spatially limited (Meza et al., 2023; Weiss et al., 2004; Yan et al., 2019), hence, preferred methods for LAI mapping rely on empirical formulations from remote sensing, calibrated through indirect field scoping methods like ceptometry (R. Gao et al., 2022; Quintanilla-Albornoz et al., 2023, 2024; Wei et al., 2020; Zarate-Valdez et al., 2012).

Finally, LST, commonly derived from thermal infrared (TIR) imagery, often requires spatial aggregation to account for surface heterogeneity in complex canopies (Burchard-Levine et al., 2020; Garcia-Santos et al., 2019; K. R. Knipper et al., 2019).

TSEB model output of energy balance components (Rn, H, LE, G) are typically validated using flux measurements from the eddy covariance (EC) technique, which quantifies mass. momentum, and energy fluxes from the surface using sonic anemometers and infrared gas analyzers high-frequency data (Bambach et al., 2022; Drechsler & Kisekka, 2022; Jofre-Čekalović et al., 2022; Sánchez et al., 2021; Xu et al., 2020). However, validation requires a methodology that links EC measurements to the contributing surface area in order to extract from the imagery a similar source area of model output (Gelybó et al., 2013; Xiang et al., 2022), ensuring relevance for ET model assessment (H. Wang et al., 2016; Xiang et al., 2022). Therefore, two-dimensional surface area footprint models (Kljun et al., 2015) have been used to estimate the upwind source area influencing EC fluxes (Melton et al., 2022; Sánchez et al., 2021; Volk et al., 2023), which depends on sensor height, wind conditions, surface roughness, and stability (Schuepp et al., 1990; Xiang et al., 2022; Yi, 2008).

This study aims to evaluate the influence of almond's canopy-induced shadows on ETa estimations from the TSEB model using high-resolution sUAS imagery. TSEB-PT ETa was assessed relative to EC estimates at three sites from the Tree-crop Remote Evapotranspiration eXperiment (T-REX) (Bambach et al., 2024). Three key questions are addressed: (1) What is the variability in TSEB-PT inputs due to canopy-induced shadow filtering? (2) What is the variability in TSEB-PT ETa estimation when performing shadow filtering to TSEB inputs? (3) Are canopy-induced shadows a bias driver in sUAS imagery when estimating ETa by the TSEB-PT model?

2 Materials and Methods

2.1 Field Sites and Monitoring

Three Commercial almond orchards were monitored during the summer seasons (June–-September) of 2021 and 2022 in California’s Sacramento and Central Valleys (Figure 1) Ripperdan (OLA), Woodland (WWF), and Vacaville (VAC). The OLA site, located in Madera County, spans 160 ha, is oriented north-south, has loam to clay loam soils, and includes Nonpareil, Wood Colony, and Supareil varieties planted in plots with varying tree ages ranging from less than six years to more than ten years (planted in 2009), with a layout of 5.5 m tree spacing and 6.4 m row spacing and irrigated with two drip lines delivering 35.7 $L\ h^{-1}$ per tree. Furthermore, as this was the largest of the three sites, validation with the EC flux tower focused on a single block containing mature trees. The WWF site, located in Yolo County, spans 62 ha, is oriented north–south, has gravelly loam soils, and includes Nonpareil, Monterey, Carmel, and Butte varieties (planted in 2014), with a layout of 4.5 m tree spacing and 6.7 m row spacing and irrigated with fanjet sprinklers delivering 37 L h^{-1} per tree. The VAC site, located in Solano County, spans 55 ha, is oriented northeast–southwest, has gravelly loam soil, and includes exclusively the Independence variety (planted in 2015–2016), with a layout of 5.5 m tree spacing and 6.3 m row spacing and irrigated with two drip lines delivering 31 L h^{-1} per tree.

T-REX's leaf and canopy scale monitoring campaigns, referred to as Intensive Observation Periods (IOPs), were conducted in July and August of 2021, and July and September of 2022. AggieAir sUAS technology was deployed, including GreatBlue, a hybrid fixed-wing platform designed for long-range missions, and the DJI Matrice 300, a vertical take-off and landing (VTOL) system (flights details in Appendix A). Multispectral and thermal imagery was collected using an experimental AggieAir sUAS sensor platform (https://uwrl.usu.edu/aggieair/) and the Altum-PT sensor (MicaSense, now AgEagle Aerial Systems Inc., https://ageagle.com/). sUAS flights lasted 20-30 minutes and were conducted at three times of day (military time): during the Landsat overpass (~11:30 AM), solar noon (~12:30 PM), and mid-afternoon (~3:30 PM)—hereafter referred to as AM, SN, and PM, respectively.

EC flux towers were first deployed in May 2021 at all sites to provide accurate and continuous measurements of atmospheric turbulence and fluxes (Rn, H, LE, G, in W m^{-2}). Sensors included a net radiometer, SN-500 (Apogee Instruments), IRGASON (Campbell Scientific) 3D sonic anemometer and fast response water vapor/CO2 sensor, EE08 temperature/humidity probe in aspirated shield TS-100 (Apogee Instruments), HFT-3 (Radiation Energy Balance System), Type E soil thermocouples, CS655 (Campbell Scientific) water content reflectometer, and PS-1 (METER) pressure switch detecting irrigation were also installed to measure ground heat flux density. Complementary, indirect ground-based LAI was measured by LAI-2200C plant canopy analyzers, and infrared thermometers (IRTs, SI-121-SS, Apogee Instruments, Inc. Logan, UT, USA) were set up for sUAS thermal image calibration.

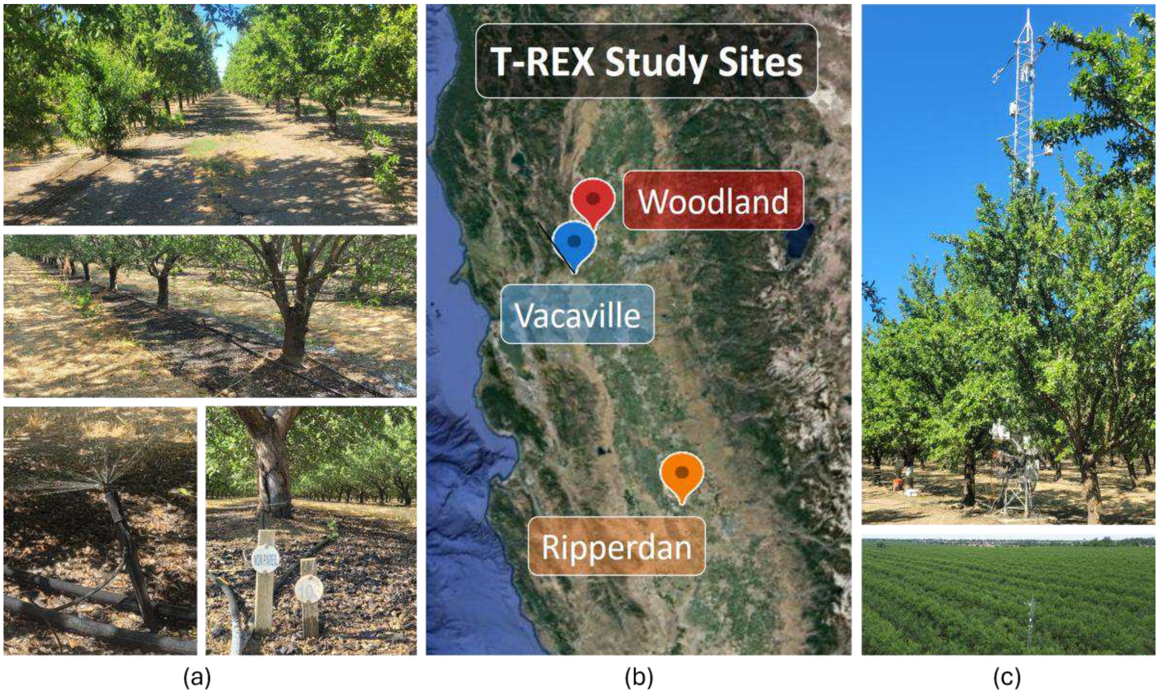

Figure 1. (a) Micro-sprinkler and drip irrigation systems in almond sites covered along by canopy shadows. (b) World imagery of the three sites of study in the Central Valley. (c) Eddy-Covariance towers with instrumentation installed in Vacaville (top) and Woodland (bottom).

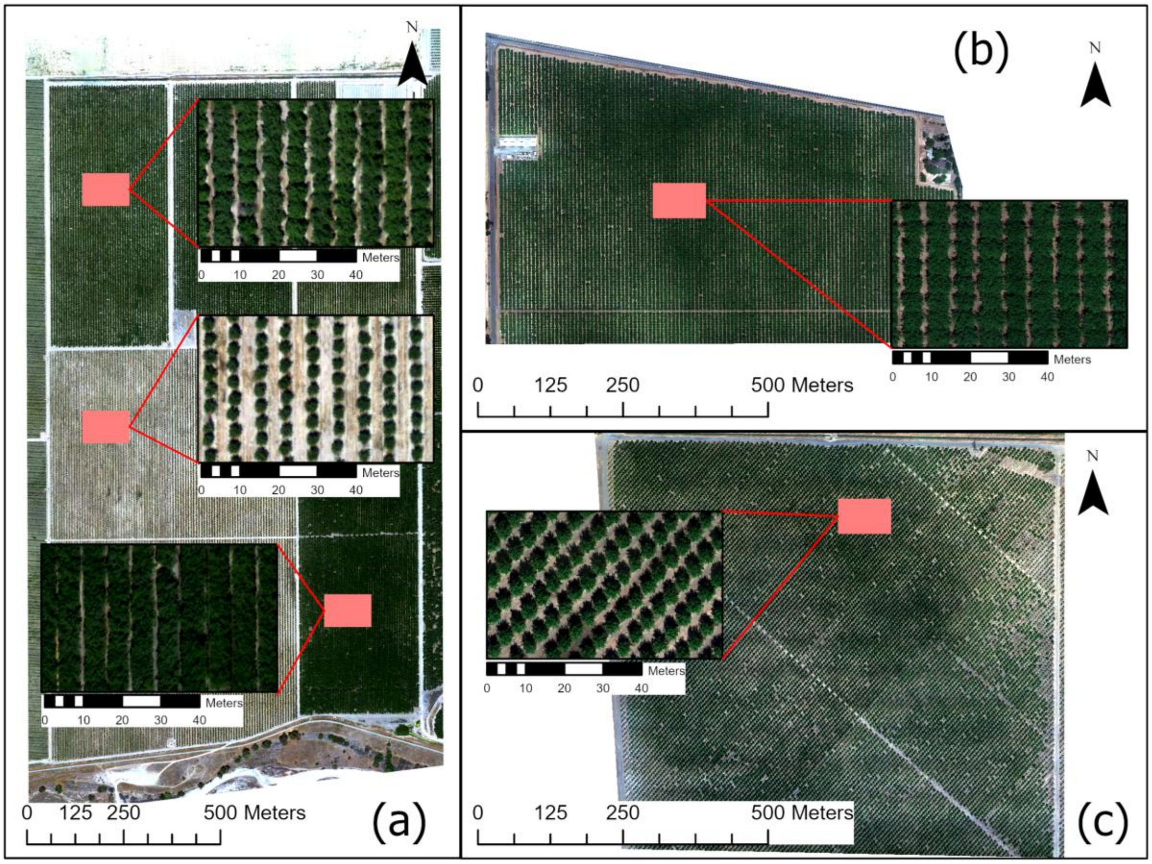

Figure 2. High resolution imagery captured for each site, (a) Ripperdan-OLA, (b) Woodland-WWF, and (c) Vacaville-VAC, by AggieAir in 2022 IOP 1.

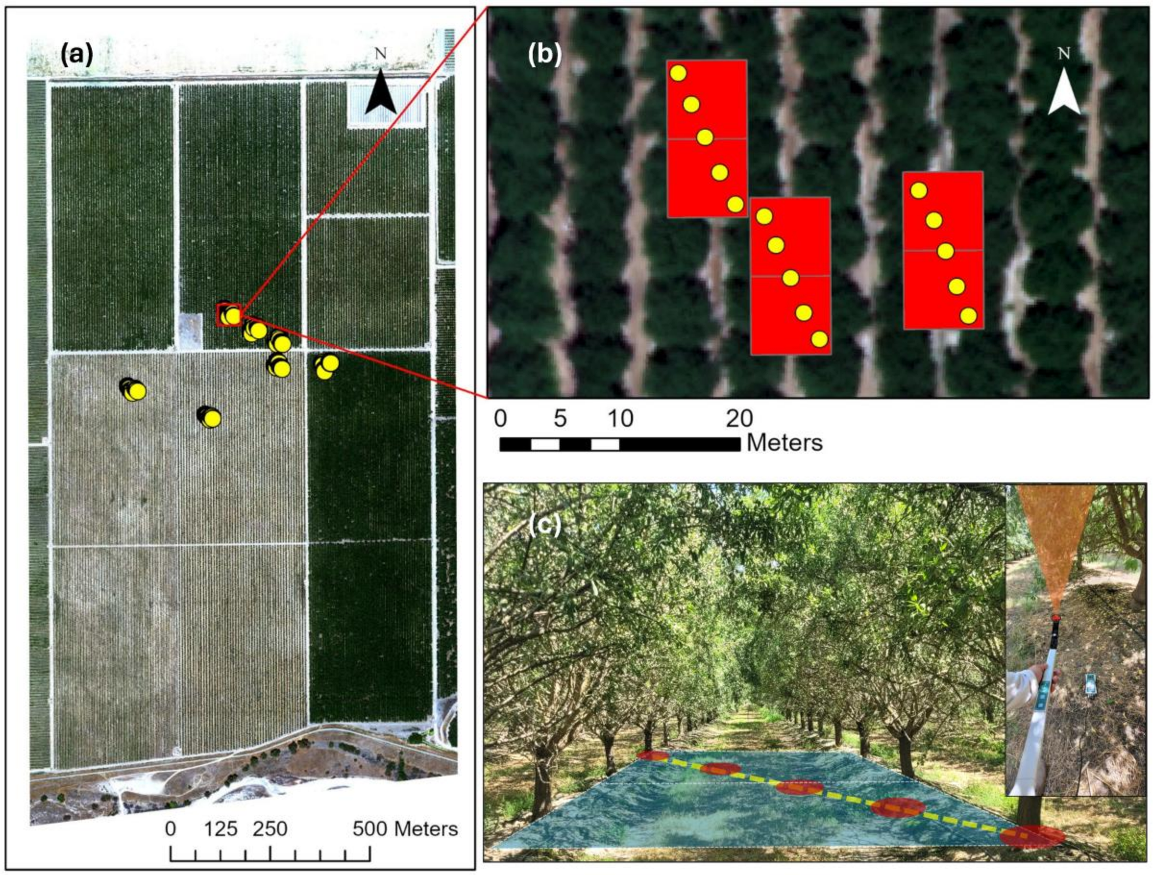

Figure 3. (a) Leaf area sampling locations in OLA site, (b) measuring LAI according to the transect method, where (c) five measurement points represent two grids of 6.5 m (resampled pixels).

2.2 Shadow filtering in sUAS imagery

sUAS imagery datasets were collected during the 2021 and 2022 IOPs and were geographically and radiometrically corrected prior to photogrammetry. Orthorectified reflectance imagery (orthomosaics) for each band (RGB, RE, NIR, and TIR) and digital surface models (DSMs) were generated from high-density point cloud data (40 points m^{-2}) as well as Normalized Difference Vegetation Index (NDVI) maps. These orthomosaics were post-processed in a GIS environment to obtain spatial TSEB-PT inputs (FC, H_{tree}, W/H_{tree}, LAI and LST) using State Plane Coordinate Systems (SPCS): NAD 1983 Zone III (2011, meters) for OLA, and NAD 1983 Zone II (2011, meters) for WWF and VAC. Imagery detail in Figure 2.

Shaded relief rasters representing canopy-induced shadows were produced for each flight dataset using the Hillshade tool (Esri. ArcGIS Pro Tool. Spatial Analyst—Hillshade), a spatial analysis function for shadow projection. This technique achieved 87% accuracy (Aboutalebi et al., 2019), based on canopy structure from DSMs, terrain features, and solar azimuth and altitude at flight time. Shaded relief rasters were used as shadow masks to filter out shadowed pixels from the orthomosaics (RGB, RE, NIR, TIR, and NDVI). As a result, each flight produced two sets of imagery: the original imagery datasets (OR) and one with shadow filtering (SF) applied.

NDVI maps were analyzed using a supervised classification approach based on a support vector machine (SVM) classifier (Esri. ArcGIS Pro Tool. Spatial Analyst—Support Vector Machine) to identify thresholds for canopy, interrow, and bare soil cover and enabled canopy delineation on the orthomosaics, achieving approximately 94% accuracy in previous studies (Aboutalebi et al., 2019; Dennison et al., 2019; L. Gao et al., 2020).

TSEB-PT inputs were derived through a data aggregation process at 6.5 m resolution to account for spatial heterogeneity and tree density (Nassar et al., 2020). This scale matches the average row spacing in almond orchards and effectively represents sUAS-derived data at the tree scale (Bellvert et al., 2018; Nieto et al., 2019; Volk et al., 2023).

Based on the canopy-delineated NDVI maps, FC was estimated as the ratio of the delineated canopy area to the aggregated pixel resolution (Aboutalebi et al., 2019; Dennison et al., 2019; L. Gao et al., 2020). Dividing FC by the aggregated pixel size yielded a representative canopy width (W) per tree (Aboutalebi et al., 2019; L. Gao et al., 2020; Nassar et al., 2020). H_{tree} was calculated as the 95th percentile value—representing treetops—from the canopy-delineated NDVI and DSM maps (Aboutalebi et al., 2019; L. Gao et al., 2020; Nassar et al., 2020), enabling the derivation of W/H_{tree} maps. LST maps were generated by averaging values from TIR-calibrated images at the aggregated resolution. TIR calibration (IRT calibration equation in Appendix B) was based on in-field IRT measurements from three reference surfaces (white, black, and ground) (Aboutalebi et al., 2019; L. Gao et al., 2020; Nassar et al., 2020).

Previous research has indicated that canopy geometry features should be integrated into the analysis of LAI for tree crops (Comba et al., 2020; Parry et al., 2019; Quintanilla-Albornoz et al., 2024). Moreover, existing empirical LAI models in almonds orchards based on vegetation indices exist (Zarate-Valdez et al., 2012). However, these were formulated using satellite multispectral sensors, which often do not correlate with the bands from commercial multispectral cameras for sUAS, failing to accurately predict LAI (Section 3.2). Therefore, for LAI map generation, an empirical equation was developed using aggregated sUAS data from non-thermal orthomosaics (RGB, RE, NIR, NDVI), FC maps, and a machine learning algorithm in Eureqa software (Nutonian Inc.). Eureqa has been used in prior studies to derive mathematical models for LAI estimation across various crops (R. Gao et al., 2022; Tunca et al., 2022; J. Wu et al., 2023). The LAI equation was calibrated using indirect measurements from LAI-2200C plant canopy analyzers, collected using a transect method as described by White et al. (2019). Lastly, TSEB-PT inputs were generated for each imagery set (OR and SF), except LAI maps, which were generated per flight day with OR datasets at SN time (R. Gao et al., 2022; Quintanilla-Albornoz et al., 2024).

Differences between the two inputs with and without shadows were assessed using the coefficient of determination (R^2), root mean square error (RMSE), mean absolute error (MAE), mean absolute percentage error (MAPE), and p-value. A one-way ANOVA was also conducted to evaluate the effects of site (OLA, VAC, WWF) and time of day (AM, SN, PM) on ΔLST ($\Delta LST = LST_{OR} - LST_{SF}$) and shadow cover ($m^2\ m^{-2}$).

2.3 TSEB-PT modeling and flux EC tower footprint method

The Priestley-Taylor formulation of the Two-Source Energy Balance (TSEB-PT) model was implemented in Python within a Jupyter environment, as applied in previous studies across various crops (R. Gao et al., 2023; Kustas et al., 2019; Meza et al., 2023), with a permanent Github repository at https://github.com/hectornieto/pyTSEB. The model integrated TSEB inputs derived from sUAS imagery and ancillary flight-time data, including location, time, weather conditions, and solar radiation. Energy balance component maps—Rn, H, LE and G—were generated for each sUAS dataset under both treatments (OR and SF).

Instantaneous two-dimensional footprint modeling developed by Kljun et al. (2015) was applied to estimate the upwind surface areas contributing to fluxes measured by the eddy covariance (EC) tower (Melton et al., 2022; Sánchez et al., 2021; Volk et al., 2023). Measurements and methodology for footprint modeling followed recommendations by Bambach et al. (2022), which included air temperature, humidity, atmospheric pressure, wind speed, and direction, standard deviation of vertical wind speed, friction velocity (u^*), and Monin-Obukhov length, derived from hourly EC tower data, along with surface roughness.

Energy imbalance in the EC measurements was addressed using Bowen ratio closure to reconcile Equation Equation 1Equation 1Equation 1 (Aboutalebi et al., 2019; Niu et al., 2020; Ortega-Farías et al., 2016; Twine et al., 2000) prior to comparison with TSEB-PT outputs.

$$Rn - G \neq LE + H \qquad \text{Equation 1}$$

Available energy (A) is defined in Equation Equation 2. Based on this, the Bowen ratio is then calculated as shown in Equation 3 and is used to adjust latent and sensible heat fluxes (Equations 4 and 5).

$$A = Rn - G \qquad \text{Equation 2}$$

$$\beta = \frac{H}{LE} \qquad \text{Equation 3}$$

$$LE_{corrected} = \frac{A}{1+\beta} \qquad \text{Equation 4}$$

$$H_{corrected} = \frac{\beta A}{1+\beta} \qquad \text{Equation 5}$$

Model performance for LE was evaluated based on the R^2, RMSD, MAE, and MAPE, statistical parameters.

3 Results and Discussion

3.1 Shadow filtering influence in TSEB inputs

TSEB-PT input maps (FC, H_{tree}, W/H_{tree}, LST) were generated for all datasets and evaluated by time of day (AM, SN, PM) as shown in Figure 4, including performance metrics (R^2, RMSE, MAE). Fractional cover (FC; Figure 4a1, Figure 4a2), derived from NDVI-based canopy delineation, showed notable reductions when shadows were filtered. In the afternoon imagery (PM datasets), FC decreased by 10–60% for initial values ranging from 0.40 to near full coverage. In the AM and SN datasets, reductions were smaller but still significant (10–20%) for FC values between 0.40 and 0.80. Canopy height (H_{tree}; Figure 4b1, Figure 4b2) showed no variation across treatments and times of day. The use of the 95th percentile mitigates shadow effects, as it primarily reflects canopy tops where shadows are least prevalent (Aboutalebi et al., 2019; Bellvert et al., 2021; Guimarães et al., 2023).

The width-to-height ratio (W/H_{tree}; Figure 4c1, Figure 4c2), derived from FC and H_{tree}, was affected by shadow filtering due to its dependence on NDVI-based delineation. Reductions were more pronounced in the AM and PM datasets. Mature trees typically exhibit W/H_{tree} ratios between 0.80 and 1.20 (Drechsler et al., 2022; Pope et al., 2016); within this range, shadow-filtered (SF) estimates dropped by up to 50% compared to original (OR) estimates.

LST estimations (Figure 4d1, Figure 4d2) increased with shadow filtering, driven by the removal of cooler pixels from shaded leaves and soil. The largest increases occurred in SN datasets, with temperature differences up to 5°C. (Aboutalebi et al., 2022) described this thermal mixture effect, where coarse or heterogeneous pixels blend thermal information from soil, vegetation, and shaded components. This highlights the significant role of shadow occurrence in LST aggregation, particularly in areas with moderate FC (0.40–0.80). Moreover, as (Lu et al., 2022) demonstrated, shaded pixels can mislead land cover classification and result in substantial discrepancies in LST estimates—up to 88% more accurate when shaded regions are included—particularly during morning and afternoon hours when sunlit–shaded contrasts are greatest.

Changes in FC were evaluated in relation to shadow cover ($m^2\ m^{-2}$; Figure 5a) and ΔLST ($\Delta LST = LST_{OR} - LST_{SF}$, °C; Figure 5b) across sites. At all sites and times of day, shadow cover increased with FC up to 0.50, after which both open areas and shadow occurrence in sUAS imagery decreased. Similarly, in the FC range of 0.20–0.50, ΔLST became increasingly negative, indicating warmer LST_{SF} compared to LST_{OR}, especially during SN and PM. These dynamics reflect the dependency of FC and LST accuracy on tree geometry (e.g., canopy height, width-height ratio, LAI) and its delineation, where shaded pixels—particularly under dense or mature canopy—can be cooler than sunlit leaves (Lu et al., 2022).

Additionally, a one-way ANOVA was performed on shadow cover and ΔLST to assess differences by time of day (Figure 6, top) and site (Figure 6, bottom). The VAC site showed the highest average shadow cover across all times, along with the highest ΔLST, likely due to its diagonal row orientation. In all cases, $F_{cal} \gg F_{crit}$, indicating statistically significant differences among times of day and sites.

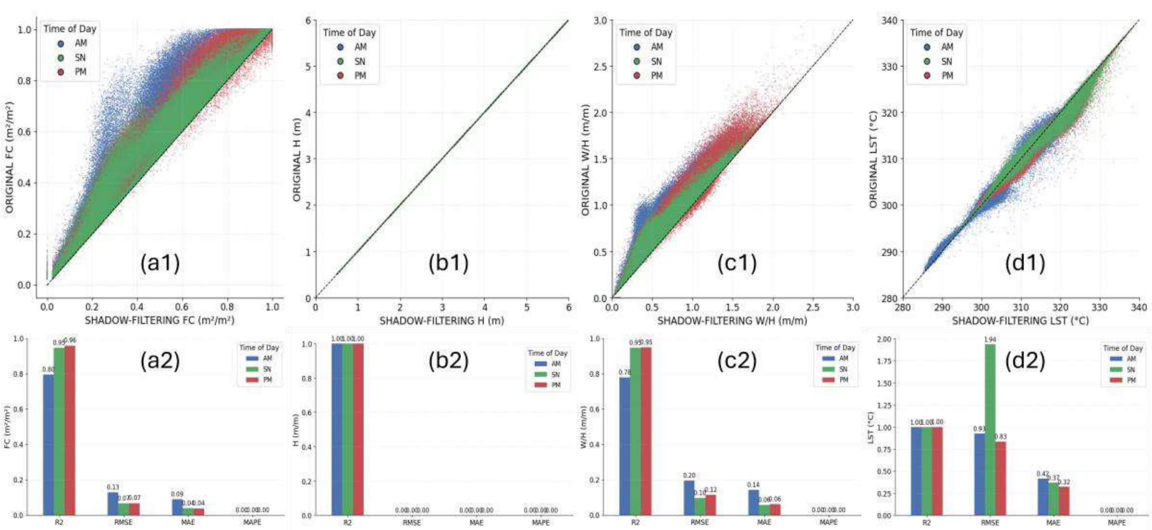

Figure 4. Comparison between OR and SF treatments, per-time of day (mid-morning, AM; solar noon, SN; mid-afternoon, PM), using sUAS-based estimations for (a1, a2) fractional cover (FC, $m^2\ m^{-2}$), (b1, b2) canopy height (H_{tree}, m), (c1, c2) width-to-height ratio (W/H_{tree}, $m\ m^{-1}$), and (d1, d2) land surface temperature (LST, °C) across all datasets with statistics (R^2, RMSE, MAE).

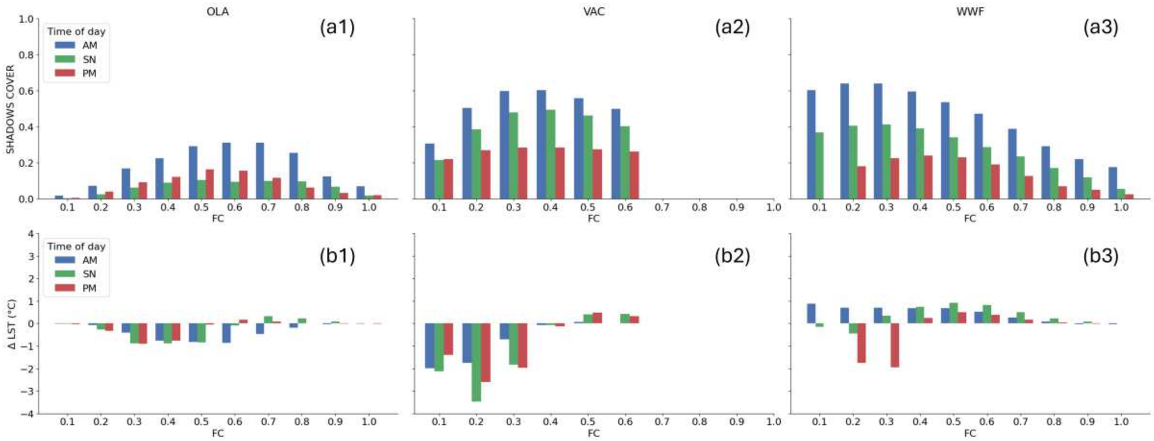

Figure 5. Bar plots showing the relationship between changes in fractional cover (FC) with (a) shadow cover (in 0.1 increments) and (b) temperature difference ($\Delta LST = LST_{OR} - LST_{SF}$, °C), for each site—OLA (a1, b1), VAC (a2, b2), and WWF (a3, b3)—with time of day differentiated.

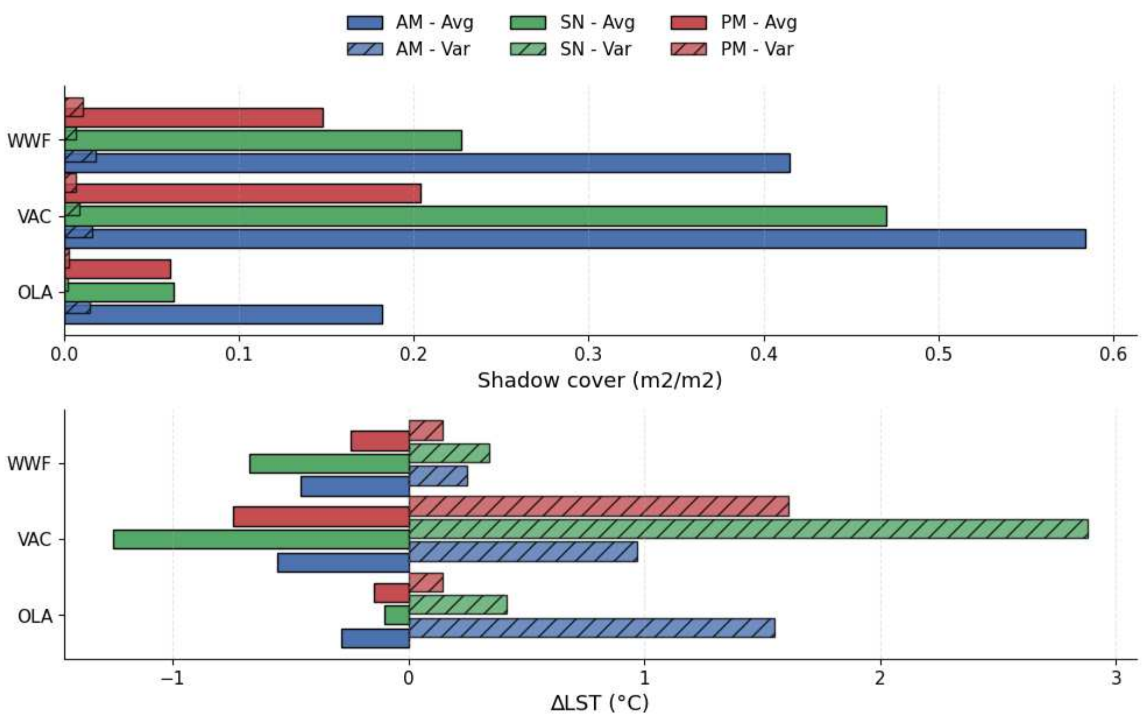

Figure 6. Bar plots showing the average (solid bars) and variance (dashed bars) of (bottom) ΔLST (°C) and (top) shadow cover (m^2 m^{-2}), based on one-way ANOVA analysis per site and time of day.

3.2 LAI modeling for sUAS data

An LAI empirical model (Equation 6) was developed based on integrating physical tree characteristics as predictors (Comba et al., 2020; Parry et al., 2019) through the Eureqa algorithm model, with $R^2 = 0.68$, and validation by indirect measurements from LAI-2200C plant canopy analyzers. Original treatment (OR) imagery datasets from AM and SN were employed for canopy delineation to ensure the minimal bias induced by shadows into the reflectance bands data aggregation (R. Gao et al., 2022; Quintanilla-Albornoz et al., 2024).

Existing empirical LAI models based on satellite information tended to overestimate LAI values (Figure 7, left). This discrepancy may be attributed to the calibration protocol and sampling methodology, which did not account for the transect-interrow effect in final data aggregation (Zarate-Valdez et al., 2012), thereby leading to discrepancies between modeled and observed LAI values.

For the evaluated dataset, which included measurements from both young and mature trees, expected LAI values in fully covered canopies of commercial almond orchards range from 2 to 3.5 m^2 m^{-2} (Figure 7, right).

Additionally, uncertainties in canopy structure, and different almond varieties used for model calibration could further influence LAI estimation. The pseudo-code for the implementation of this equation from sUAS information is presented in Appendix C.

$$LAI = \frac{NDVI - 2.4631}{FC - 1.4726} \qquad \text{Equation 6}$$

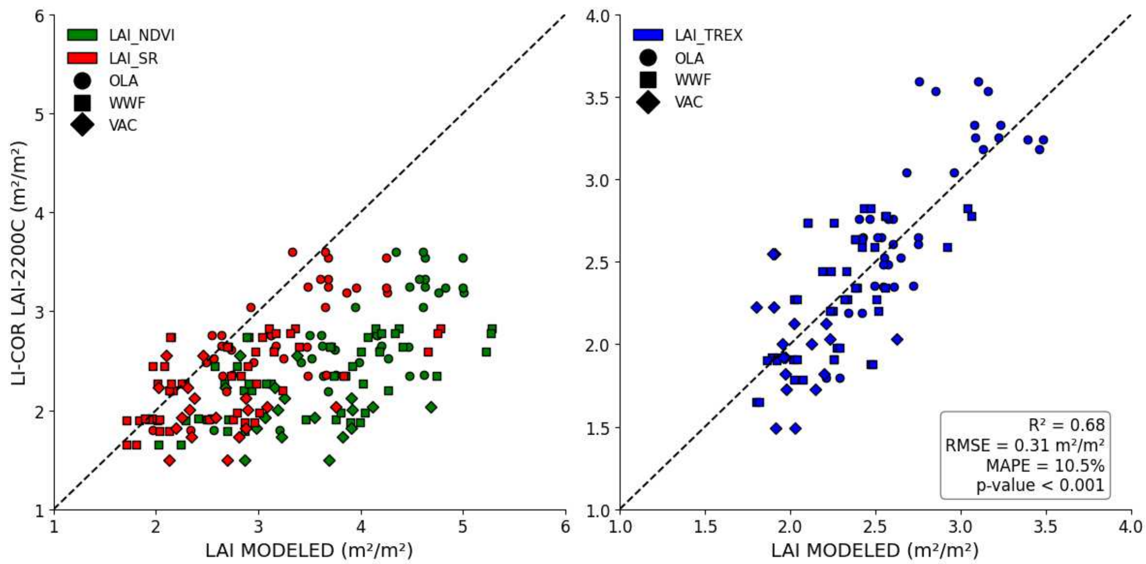

Figure 7. Comparison between (left) previously published LAI models based on vegetation indices and (right) the proposed empirical model (Equation 6), developed using sUAS-based information and validated with LAI-2200C plant canopy analyzer measurements. Relevant statistical metrics are presented.

3.3 Impact of TSEB-derived LE due to shadow filtering

LE estimates from the two treatments (OR and SF) were compared by time of day (Figure 8a). Results show a clear influence of shadow removal, particularly at SN and, in some cases, PM, where LE estimates significantly decreased. Correlation between treatments (Figure 8d) was strongest at AM and SN (R^2 = 0.91), while RMSE ranged from 67 to 143 W m^{-2} and MAE from 38 to 123 m^{-2} across all datasets.

By site (Figure 8b), WWF showed stronger agreement between treatments, whereas OLA and VAC exhibited more pronounced LE reductions after shadow filtering.

Figure 8c illustrates LE estimates colored by FC, revealing that lower FC (below 0.4) was associated with larger LE drops under shadow filtering—primarily in younger orchards. OLA and VAC sites contained younger trees with low FC, while WWF had mostly mature trees with high FC (above 0.8), leading to better agreement.

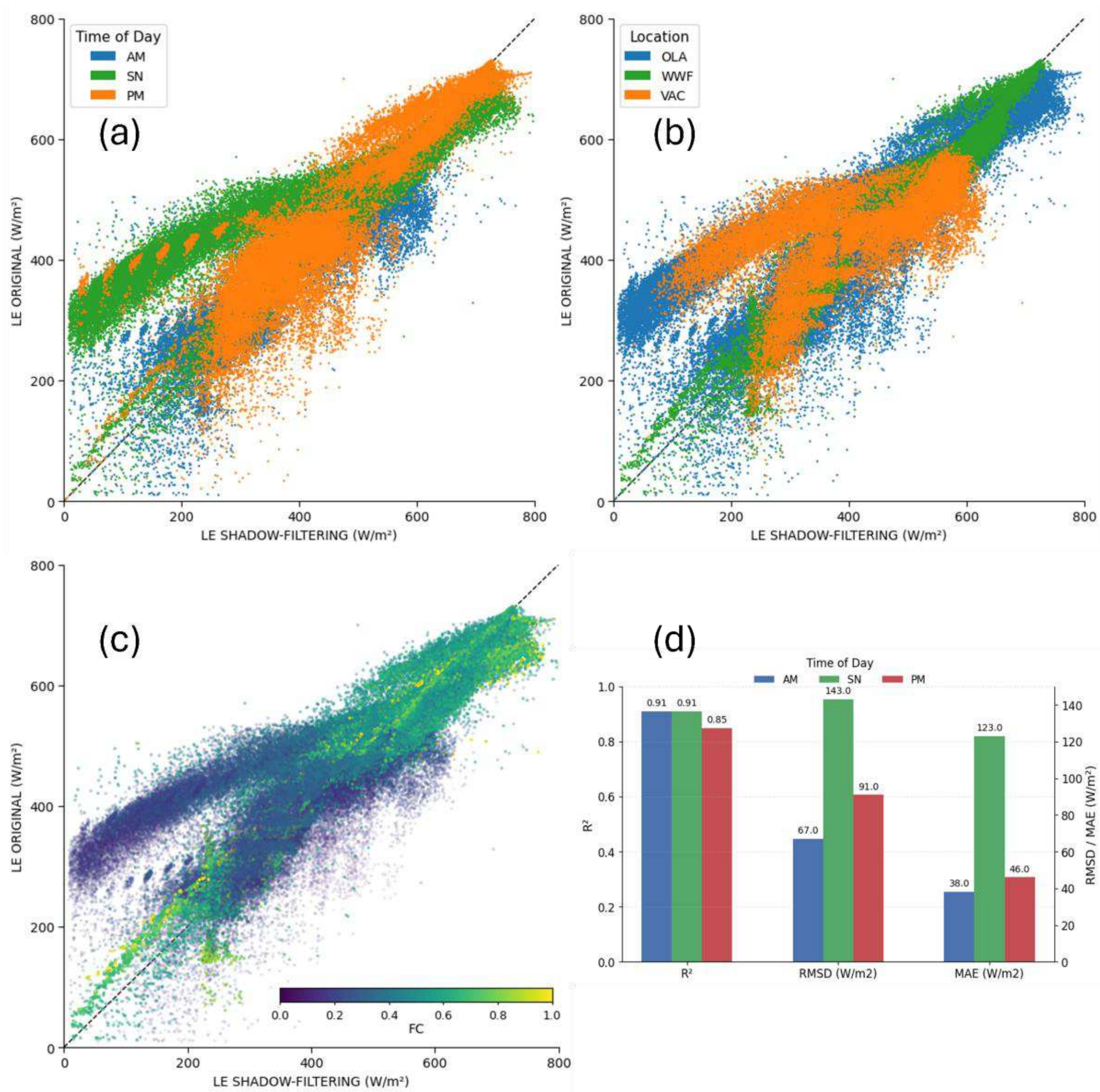

Figure 8. Comparison of latent heat flux estimations from TSEB-PT treatments: the x-axis represents shadow-filtered values and the y-axis original values. The analysis is presented by differentiation by (a) time of day, (b) site, (c) variation in fractional cover (FC, shown as a color bar), and (d) main statistical metrics per time of day.

3.4 Validation of TSEB computed LE using estimated flux footprint method

LE validation from TSEB-PT was performed using the footprint approach and EC tower measurements, with Bowen ratio closure correction (Equations 4 and 5) (Kustas et al., 2019; Nieto et al., 2019; Sánchez et al., 2021; Twine et al., 2000; Vulova et al., 2021), at each site. This approach preserves the physically grounded partitioning of sensible and latent heat, enabling consistent comparison between sUAS-based TSEB fluxes and EC data. Weighted footprints were estimated using the (Kljun et al., 2015) model, following the recommendations of (Bambach et al., 2022). Figure 9 shows the pink footprint contours over some of the instantaneous LE maps from the OR dataset.

LE estimates from both OR and SF inputs were compared to corrected EC tower data (Figure 10a). Statistical analysis showed better performance for OR across all energy balance components, with lower p-values, higher R^2, and lower RMSD, MAE, and MAPE. However, only net radiation (Rn) showed a significant correlation with EC data. Sensible heat flux (H), latent heat flux (LE), and ground heat flux (G) showed weak correlations. This is partly the result of the fluxes having small range in values. The large MAPE in H is due to the fact that the magnitude of H was generally small.

In the case of G, underestimation may be attributed to the limited observed range and the TSEB-PT formulation, which estimates G as a fraction of net radiation (Norman et al., 1995) which the fraction is likely to vary with time of day (Nieto et al., 2019). For H and LE, high dispersion may reflect limitations of the current formulation using Priestley-Taylor for canopy transpiration, which can be enhanced by alternative TSEB methods (Nieto et al., 2019).

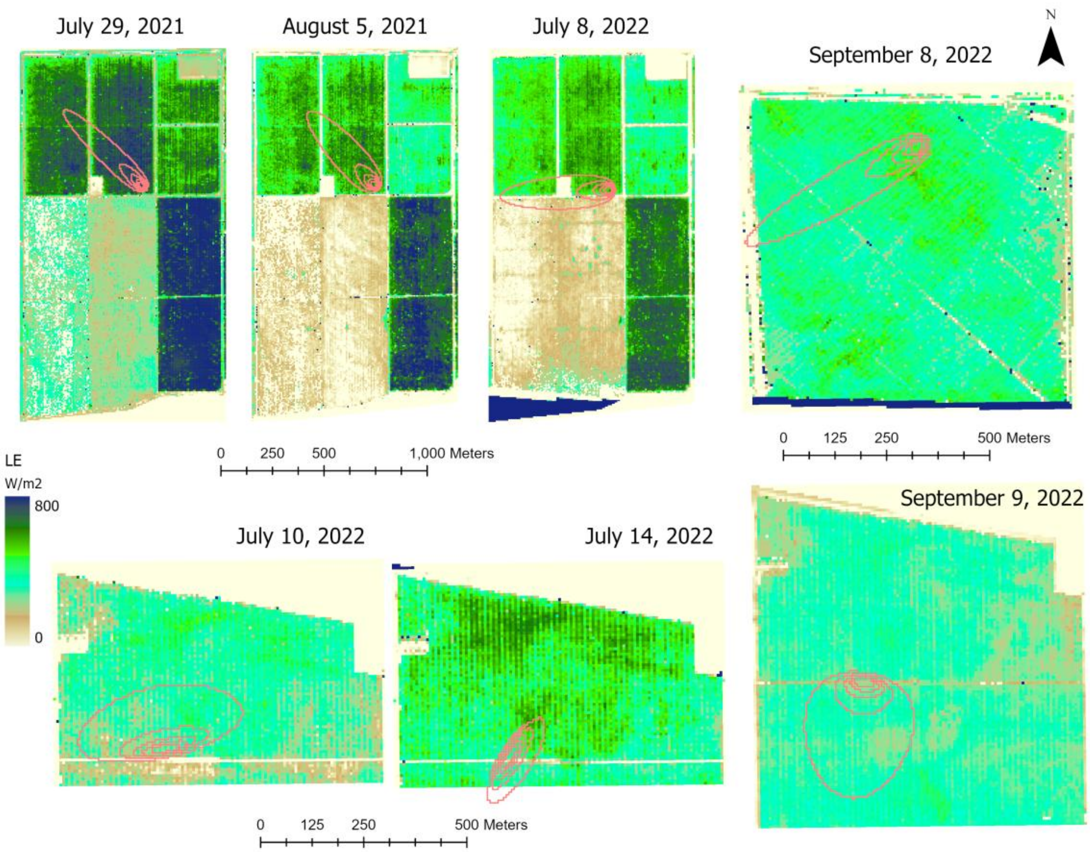

Figure 9. Samples of seven different latent heat flux (LE) maps (in W m^{-2}) across the three sites at solar noon. The date is indicated for each map, and the hourly weighted footprint estimated for each eddy covariance (EC) tower position is included (pink line).

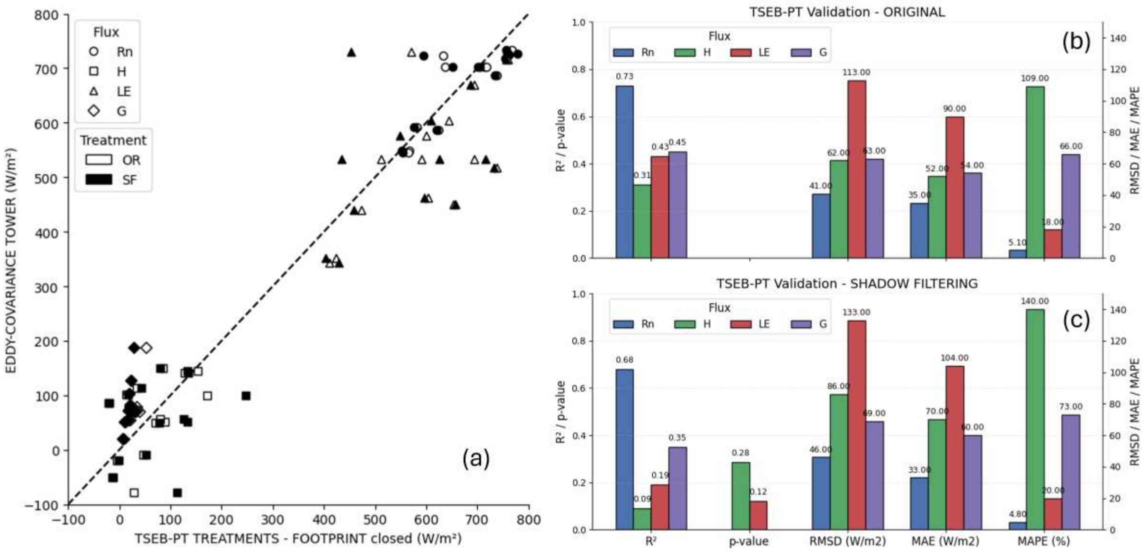

Figure 10. Validation of eddy covariance flux measurements (Rn, H, LE, G) using footprint technique and Bowen ratio energy balance closure correction for (a) TSEB-PT estimations. Statistical metrics (R^2, p-value, RMSD, MAE, MAPE), per energy balance component, are presented for (b) original (OR) and (c) shadow-filtering (SF) treatments.

4 Conclusions

Canopy-induced shadows introduced bias in the estimation of land surface properties by affecting canopy delineation and altering shortwave reflectance due to changes in surface albedo. Consequently, canopy geometry features such as fractional cover (FC), width-to-height ratio (W/H_{tree}), and leaf area index (LAI), derived from sUAS-based imagery, are significantly impacted by shadow filtering. To minimize these effects, canopy geometry should be estimated using imagery acquired near solar noon, when shadow occurrence is minimal.

A sUAS-based LAI model ($R^2 = 0.68$), developed using low-shadow imagery and based on FC and NDVI, improved estimation accuracy. LAI values ranged from 1.5 to 3.7 $m^2\ m^{-2}$, underscoring the importance of incorporating canopy structure in orchard-specific models.

Shadow filtering in TSEB-PT inputs significantly affected latent heat flux (LE) estimates, particularly for orchards with FC between 0.40 and 0.80, typical of young to early-mature trees. While filtering enables the separation of sunlit and shaded components—each with distinct energy balances—both contribute to the composite flux. Thus, shadow presence influences LST by aggregating cooling effects across the orchard and should be preserved in energy balance modeling.

LST can be estimated throughout the daylight period for instantaneous ETa modeling, and shaded pixels should not be excluded, as TSEB-PT LE estimates aligned more closely with EC observations when shadows were retained. To support accurate canopy delineation for other TSEB inputs, LST should be combined with shortwave data acquired during minimal shadowing—preferably at solar noon. For flux modeling across different times of day, the TSEB-2TQ approach (R. Gao et al., 2023) provides a robust framework for correcting temperature inputs.

Few studies have assessed the impact of excluding shaded pixels at different times of day on TSEB inputs in tree crops. Evaluating this under the TSEB-PT approach helps establish a baseline for how shadow exclusion affects basic inputs and model performance, which enhances under more advance formulations

(R. Gao et al., 2023; Nieto et al., 2019). Additionally, other technologies such as LiDAR can help mitigate shadow-related limitations in sUAS imagery by providing accurate geometric inputs for TSEB.

This study advances the application of TSEB with sUAS for ETa estimation by improving the understanding of data behavior, thereby supporting further research on E/T partitioning and water stress in almond orchards. Continued integration of the methodologies proposed here will facilitate more complex analyses, including evaluation of TSEB performance under varying climatic conditions, particularly during hot, dry air advection.

Acknowledgments

This research is framed in the Tree Crop Remote Sensing of Evapotranspiration Experiment (T-REX) project, funded by the Almond Board of California [project WATER16], the California Department of Food and Agriculture (CFDA) Specialty Crops Block Grant Program, and USDA-CRIS base funds. We appreciate the UC Davis-USDA ARS Crop Sensing Group for sensors array and physiological data collection and AggieAir Service Center for UAS data collection and processing of the different flights in 2021 and 2022. Particularly, we thank Dr. Hector Nieto (Institute of Agricultural Sciences, ICA-CSIC, Spain) for his valuable contributions to the model framework and graphical user interface, as well as for developing key components of the processing pipeline.

Statements and Declarations

Competing Interests: The authors declare no competing interests.

Funding: This study was funded by the Almond Board of California.

Author Contributions: All authors contributed to study design, data collection, analysis, and manuscript preparation.

References

Aboutalebi, M., Torres-Rua, A. F., McKee, M., Kustas, W. P., Nieto, H., Alsina, M. M., White, A., Prueger, J. H., McKee, L., Alfieri, J., Hipps, L., Coopmans, C., Sanchez, L., & Dokoozlian, N. (2022). Downscaling UAV land surface temperature using a coupled wavelet-machine learning-optimization algorithm and its impact on evapotranspiration. *Irrigation Science*, *40*(4–5), 553–574. https://doi.org/10.1007/s00271-022-00801-2

Aboutalebi, M., Torres-Rua, A., Kustas, W. P., Nieto, H., Coopmans, C., & McKee, M. (2019). Assessment of different methods for shadow detection in high-resolution optical imagery and evaluation of shadow impact on calculation of NDVI, and evapotranspiration. *Irrigation Science*, *37*(3), 407–429. https://doi.org/10.1007/s00271-018-0613-9

Agam, N., Kustas, W. P., Anderson, M. C., Norman, J. M., Colaizzi, P. D., Howell, T. A., Prueger, J. H., Meyers, T. P., & Wilson, T. B. (2010). Application of the Priestley–Taylor Approach in a Two-

Source Surface Energy Balance Model. *Journal of Hydrometeorology*, *11*(1), 185–198. https://doi.org/10.1175/2009JHM1124.1

Ali, A., & Imran, M. (2020). Evaluating the potential of red edge position (REP) of hyperspectral remote sensing data for real time estimation of LAI & chlorophyll content of kinnow mandarin (Citrus reticulata) fruit orchards. *Scientia Horticulturae*, *267*, 109326. https://doi.org/10.1016/j.scienta.2020.109326

Allen, R. G., Tasumi, M., & Trezza, R. (2007). Satellite-Based Energy Balance for Mapping Evapotranspiration with Internalized Calibration (METRIC)—Model. *Journal of Irrigation and Drainage Engineering*, *133*(4), 380–394. https://doi.org/10.1061/(ASCE)0733-9437(2007)133:4(380)

Anderson, M. C., Kustas, W. P., Norman, J. M., Diak, G. T., Hain, C. R., Gao, F., Yang, Y., Knipper, K. R., Xue, J., Yang, Y., Crow, W. T., Holmes, T. R. H., Nieto, H., Guzinski, R., Otkin, J. A., Mecikalski, J. R., Cammalleri, C., Torres-Rua, A. T., Zhan, X., … Agam, N. (2024). A brief history of the thermal IR-based Two-Source Energy Balance (TSEB) model – diagnosing evapotranspiration from plant to global scales. *Agricultural and Forest Meteorology*, *350*, 109951. https://doi.org/10.1016/j.agrformet.2024.109951

Bambach, N., Knipper, K., McElrone, A. J., Nocco, M., Torres-Rua, A., Kustas, W., Anderson, M., Castro, S., Edwards, E., Duran-Gomez, M., Gal, A., Tolentino, P., Wright, I., Roby, M., Gao, F., Alfieri, J., Prueger, J., Hipps, L., & Saa, S. (2024). The Tree-Crop Remote Sensing of Evapotranspiration Experiment (T-REX): A Science-Based Path for Sustainable Water Management and Climate Resilience. *Bulletin of the American Meteorological Society*, *105*(1), E257–E284. https://doi.org/10.1175/BAMS-D-22-0118.1

Bambach, N., Kustas, W., Alfieri, J., Prueger, J., Hipps, L., McKee, L., Castro, S. J., Volk, J., Alsina, M. M., & McElrone, A. J. (2022). Evapotranspiration uncertainty at micrometeorological scales: The impact of the eddy covariance energy imbalance and correction methods. *Irrigation Science*, *40*(4–5), 445–461. https://doi.org/10.1007/s00271-022-00783-1

Bastiaanssen, W. G. M., Menenti, M., Feddes, R. A., & Holtslag, A. A. M. (1998). A remote sensing surface energy balance algorithm for land (SEBAL). 1. Formulation. *Journal of Hydrology*, *212–213*, 198–212. https://doi.org/10.1016/S0022-1694(98)00253-4

Bellvert, J., Adeline, K., Baram, S., Pierce, L., Sanden, B., & Smart, D. (2018). Monitoring Crop Evapotranspiration and Crop Coefficients over an Almond and Pistachio Orchard Throughout Remote Sensing. *Remote Sensing*, *10*(12), 2001. https://doi.org/10.3390/rs10122001

Bellvert, J., Nieto, H., Pelechá, A., Jofre-Čekalović, C., Zazurca, L., & Miarnau, X. (2021). Remote Sensing Energy Balance Model for the Assessment of Crop Evapotranspiration and Water Status in an Almond Rootstock Collection. *Frontiers in Plant Science*, *12*, 608967. https://doi.org/10.3389/fpls.2021.608967

Burchard-Levine, V., Borra-Serrano, I., Peña, J. M., Kustas, W. P., Guerra, J. G., Dorado, J., Mesías-Ruiz, G., Herrezuelo, M., Mary, B., McKee, L. M., De Castro, A. I., Sanchez-Élez, S., & Nieto, H. (2025). Evaluating the precise grapevine water stress detection using unmanned aerial vehicles and evapotranspiration-based metrics. *Irrigation Science*, *43*(1), 65–85. https://doi.org/10.1007/s00271-024-00931-9

Burchard-Levine, V., Nieto, H., Riaño, D., Migliavacca, M., El-Madany, T. S., Perez-Priego, O., Carrara, A., & Martín, M. P. (2020). Seasonal Adaptation of the Thermal-Based Two-Source Energy Balance Model for Estimating Evapotranspiration in a Semiarid Tree-Grass Ecosystem. *Remote Sensing*, *12*(6), 904. https://doi.org/10.3390/rs12060904

Cheng, Z., Qi, L., Cheng, Y., Wu, Y., & Zhang, H. (2020). Interlacing Orchard Canopy Separation and Assessment using UAV Images. *Remote Sensing*, *12*(5), 767. https://doi.org/10.3390/rs12050767

Comba, L., Biglia, A., Ricauda Aimonino, D., Tortia, C., Mania, E., Guidoni, S., & Gay, P. (2020). Leaf Area Index evaluation in vineyards using 3D point clouds from UAV imagery. *Precision Agriculture*, *21*(4), 881–896. https://doi.org/10.1007/s11119-019-09699-x

Davidson, A. M., Le, S. T., Cooper, K. B., Lange, E., & Zwieniecki, M. A. (2021). No time to rest: Seasonal dynamics of non-structural carbohydrates in twigs of three Mediterranean tree species suggest year-round activity. *Scientific Reports*, *11*(1), 5181. https://doi.org/10.1038/s41598-021-83935-1

Dennison, P. E., Qi, Y., Meerdink, S. K., Kokaly, R. F., Thompson, D. R., Daughtry, C. S. T., Quemada, M., Roberts, D. A., Gader, P. D., Wetherley, E. B., Numata, I., & Roth, K. L. (2019). Comparison of Methods for Modeling Fractional Cover Using Simulated Satellite Hyperspectral Imager Spectra. *Remote Sensing*, *11*(18), 2072. https://doi.org/10.3390/rs11182072

Drechsler, K., Fulton, A., & Kisekka, I. (2022). Crop coefficients and water use of young almond orchards. *Irrigation Science*, *40*(3), 379–395. https://doi.org/10.1007/s00271-022-00786-y

Drechsler, K., & Kisekka, I. (2022). Variety specific irrigation of almonds during hull split, effects on yield and quality. *Agricultural Water Management*, *271*, 107770. https://doi.org/10.1016/j.agwat.2022.107770

Duncan, R. A., Gordon, P. E., Holtz, B. A., Zuber, C., Rijal, J., Murdock, J., Long, P., & Goodrich, B. (2024). *Sample Costs to Establish an Orchard and Produce Self Fertile Almonds, San Joaquin Valley North, Micro-Sprinkler Irrigation*.

Fulton, J., Norton, M., & Shilling, F. (2019). Water-indexed benefits and impacts of California almonds. *Ecological Indicators*, *96*, 711–717. https://doi.org/10.1016/j.ecolind.2017.12.063

Gao, L., Wang, X., Johnson, B. A., Tian, Q., Wang, Y., Verrelst, J., Mu, X., & Gu, X. (2020). Remote sensing algorithms for estimation of fractional vegetation cover using pure vegetation index values: A review. *ISPRS Journal of Photogrammetry and Remote Sensing*, *159*, 364–377. https://doi.org/10.1016/j.isprsjprs.2019.11.018

Gao, R., Torres-Rua, A. F., Aboutalebi, M., White, W. A., Anderson, M., Kustas, W. P., Agam, N., Alsina, M. M., Alfieri, J., Hipps, L., Dokoozlian, N., Nieto, H., Gao, F., McKee, L. G., Prueger, J. H., Sanchez, L., Mcelrone, A. J., Bambach-Ortiz, N., Coopmans, C., & Gowing, I. (2022). LAI estimation across California vineyards using sUAS multi-seasonal multi-spectral, thermal, and elevation information and machine learning. *Irrigation Science*, *40*(4–5), 731–759. https://doi.org/10.1007/s00271-022-00776-0

Gao, R., Torres-Rua, A. F., Nieto, H., Zahn, E., Hipps, L., Kustas, W. P., Alsina, M. M., Bambach, N., Castro, S. J., Prueger, J. H., Alfieri, J., McKee, L. G., White, W. A., Gao, F., McElrone, A. J., Anderson, M., Knipper, K., Coopmans, C., Gowing, I., … Dokoozlian, N. (2023). ET Partitioning

Assessment Using the TSEB Model and sUAS Information across California Central Valley Vineyards. *Remote Sensing*, *15*(3), 756. https://doi.org/10.3390/rs15030756

Garcia-Santos, V., Cuxart, J., Jimenez, M. A., Martinez-Villagrasa, D., Simo, G., Picos, R., & Caselles, V. (2019). Study of Temperature Heterogeneities at Sub-Kilometric Scales and Influence on Surface–Atmosphere Energy Interactions. *IEEE Transactions on Geoscience and Remote Sensing*, *57*(2), 640–654. https://doi.org/10.1109/TGRS.2018.2859182

Gebremichael, M., Krishnamurthy, P. K., Ghebremichael, L. T., & Alam, S. (2021). What Drives Crop Land Use Change during Multi-Year Droughts in California's Central Valley? Prices or Concern for Water? *Remote Sensing*, *13*(4), 650. https://doi.org/10.3390/rs13040650

Gelybó, Gy., Barcza, Z., Kern, A., & Kljun, N. (2013). Effect of spatial heterogeneity on the validation of remote sensing based GPP estimations. *Agricultural and Forest Meteorology*, *174–175*, 43–53. https://doi.org/10.1016/j.agrformet.2013.02.003

Gonzalez-Dugo, V., Testi, L., Villalobos, F. J., López-Bernal, A., Orgaz, F., Zarco-Tejada, P. J., & Fereres, E. (2020). Empirical validation of the relationship between the crop water stress index and relative transpiration in almond trees. *Agricultural and Forest Meteorology*, *292–293*, 108128. https://doi.org/10.1016/j.agrformet.2020.108128

Guimarães, N., Pádua, L., Sousa, J. J., Bento, A., & Couto, P. (2023). Almond cultivar identification using machine learning classifiers applied to UAV-based multispectral data. *International Journal of Remote Sensing*, *44*(5), 1533–1555. https://doi.org/10.1080/01431161.2023.2185913

Helalia, S. A., Anderson, R. G., Skaggs, T. H., Jenerette, G. D., Wang, D., & Šimůnek, J. (2021). Impact of Drought and Changing Water Sources on Water Use and Soil Salinity of Almond and Pistachio Orchards: 1. Observations. *Soil Systems*, *5*(3), 50. https://doi.org/10.3390/soilsystems5030050

Jha, G., Nicolas, F., Schmidt, R., Suvočarev, K., Diaz, D., Kisekka, I., Scow, K., & Nocco, M. A. (2022). Irrigation Decision Support Systems (IDSS) for California's Water–Nutrient–Energy Nexus. *Agronomy*, *12*(8), 1962. https://doi.org/10.3390/agronomy12081962

Jia, Q., & Wang, Y.-P. (2021). Relationships between Leaf Area Index and Evapotranspiration and Crop Coefficient of Hilly Apple Orchard in the Loess Plateau. *Water*, *13*(14), 1957. https://doi.org/10.3390/w13141957

Jofre-Čekalović, C., Nieto, H., Girona, J., Pamies-Sans, M., & Bellvert, J. (2022). Accounting for Almond Crop Water Use under Different Irrigation Regimes with a Two-Source Energy Balance Model and Copernicus-Based Inputs. *Remote Sensing*, *14*(9), 2106. https://doi.org/10.3390/rs14092106

Kljun, N., Calanca, P., Rotach, M. W., & Schmid, H. P. (2015). A simple two-dimensional parameterisation for Flux Footprint Prediction (FFP). *Geoscientific Model Development*, *8*(11), 3695–3713. https://doi.org/10.5194/gmd-8-3695-2015

Knipper, K., Anderson, M., Bambach, N., Melton, F., Ellis, Z., Yang, Y., Volk, J., McElrone, A. J., Kustas, W., Roby, M., Carrara, W., Castro, S., Kilic, A., Fisher, J. B., Ruhoff, A., Senay, G. B., Morton, C., Saa, S., & Allen, R. G. (2024). A comparative analysis of OpenET for evaluating evapotranspiration in California almond orchards. *Agricultural and Forest Meteorology*, *355*, 110146. https://doi.org/10.1016/j.agrformet.2024.110146

Knipper, K. R., Kustas, W. P., Anderson, M. C., Alfieri, J. G., Prueger, J. H., Hain, C. R., Gao, F., Yang, Y., McKee, L. G., Nieto, H., Hipps, L. E., Alsina, M. M., & Sanchez, L. (2019). Evapotranspiration estimates derived using thermal-based satellite remote sensing and data fusion for irrigation management in California vineyards. *Irrigation Science*, *37*(3), 431–449. https://doi.org/10.1007/s00271-018-0591-y

Kustas, W. P., Alfieri, J. G., Nieto, H., Wilson, T. G., Gao, F., & Anderson, M. C. (2019). Utility of the two-source energy balance (TSEB) model in vine and interrow flux partitioning over the growing season. *Irrigation Science*, *37*(3), 375–388. https://doi.org/10.1007/s00271-018-0586-8

Kustas, W. P., Anderson, M. C., Alfieri, J. G., Knipper, K., Torres-Rua, A., Parry, C. K., Nieto, H., Agam, N., White, W. A., Gao, F., McKee, L., Prueger, J. H., Hipps, L. E., Los, S., Alsina, M. M., Sanchez, L., Sams, B., Dokoozlian, N., McKee, M., … Hain, C. (2018). The Grape Remote Sensing Atmospheric Profile and Evapotranspiration Experiment. *Bulletin of the American Meteorological Society*, *99*(9), 1791–1812. https://doi.org/10.1175/BAMS-D-16-0244.1

Lu, S., Xuan, J., Zhang, T., Bai, X., Tian, F., & Ortega-Farias, S. (2022). Effect of the Shadow Pixels on Evapotranspiration Inversion of Vineyard: A High-Resolution UAV-Based and Ground-Based Remote Sensing Measurements. *Remote Sensing*, *14*(9), 2259. https://doi.org/10.3390/rs14092259

Maldera, F., Carone, V., Castellarnau, I. I., Vivaldi, G. A., & Camposeo, S. (2023). Available PAR, Growth and Yield of a Super High-Density Almond Orchard Are Influenced by Different Row Orientations. *Agronomy*, *13*(3), 874. https://doi.org/10.3390/agronomy13030874

Marvinney, E., Ro, J. W., & Kendall, A. (2020). Trade-Offs in Net Life Cycle Energy Balance and Water Consumption in California Almond Orchards. *Energies*, *13*(12), 3195. https://doi.org/10.3390/en13123195

McCullough-Sanden, B. L., McBride, J., Urban, D., Heilmayr, R., Kilham, N., Madgavkar, A., Lampenin, B. D., & Shackel, K. (2021). Correlation of almond yield with applied water and remotely sensed canopy temperature in the San Joaquin Valley of California. *6th Decennial National Irrigation Symposium, 6-8, December 2021, San Diego, California*. 6th Decennial National Irrigation Symposium, 6-8, December 2021, San Diego, California. https://doi.org/10.13031/irrig.2020-060

Melton, F. S., Huntington, J., Grimm, R., Herring, J., Hall, M., Rollison, D., Erickson, T., Allen, R., Anderson, M., Fisher, J. B., Kilic, A., Senay, G. B., Volk, J., Hain, C., Johnson, L., Ruhoff, A., Blankenau, P., Bromley, M., Carrara, W., … Anderson, R. G. (2022). OpenET: Filling a Critical Data Gap in Water Management for the Western United States. *JAWRA Journal of the American Water Resources Association*, *58*(6), 971–994. https://doi.org/10.1111/1752-1688.12956

Meza, K., Torres-Rua, A. F., Hipps, L., Kustas, W. P., Gao, R., Christiansen, L., Kopp, K., Nieto, H., Burchard-Levine, V., Martín, M. P., Coopmans, C., & Gowing, I. (2023). Spatial estimation of actual evapotranspiration over irrigated turfgrass using sUAS thermal and multispectral imagery and TSEB model. *Irrigation Science*. https://doi.org/10.1007/s00271-023-00899-y

Nassar, A., Torres-Rua, A., Kustas, W., Nieto, H., McKee, M., Hipps, L., Stevens, D., Alfieri, J., Prueger, J., Alsina, M. M., McKee, L., Coopmans, C., Sanchez, L., & Dokoozlian, N. (2020). Influence of Model Grid Size on the Estimation of Surface Fluxes Using the Two Source Energy Balance Model and sUAS Imagery in Vineyards. *Remote Sensing*, *12*(3), 342. https://doi.org/10.3390/rs12030342

Nieto, H., Kustas, W. P., Torres-Rúa, A., Alfieri, J. G., Gao, F., Anderson, M. C., White, W. A., Song, L., Alsina, M. D. M., Prueger, J. H., McKee, M., Elarab, M., & McKee, L. G. (2019). Evaluation of TSEB turbulent fluxes using different methods for the retrieval of soil and canopy component temperatures from UAV thermal and multispectral imagery. *Irrigation Science*, *37*(3), 389–406. https://doi.org/10.1007/s00271-018-0585-9

Niu, H., Hollenbeck, D., Zhao, T., Wang, D., & Chen, Y. (2020). Evapotranspiration Estimation with Small UAVs in Precision Agriculture. *Sensors*, *20*(22), 6427. https://doi.org/10.3390/s20226427

Norman, J. M., Kustas, W. P., & Humes, K. S. (1995). Source approach for estimating soil and vegetation energy fluxes in observations of directional radiometric surface temperature. *Agricultural and Forest Meteorology*, *77*(3–4), 263–293. https://doi.org/10.1016/0168-1923(95)02265-Y

O'Neil, C. E., Nicklas, T. A., & Fulgoni Iii, V. L. (2016). Almond Consumption Is Associated with Better Nutrient Intake, Nutrient Adequacy, and Diet Quality in Adults: National Health and Nutrition Examination Survey 2001-2010. *Food and Nutrition Sciences*, *07*(07), 504–515. https://doi.org/10.4236/fns.2016.77052

Ortega-Farías, S., Ortega-Salazar, S., Poblete, T., Kilic, A., Allen, R., Poblete-Echeverría, C., Ahumada-Orellana, L., Zuñiga, M., & Sepúlveda, D. (2016). Estimation of Energy Balance Components over a Drip-Irrigated Olive Orchard Using Thermal and Multispectral Cameras Placed on a Helicopter-Based Unmanned Aerial Vehicle (UAV). *Remote Sensing*, *8*(8), 638. https://doi.org/10.3390/rs8080638

Paciolla, N., Corbari, C., Kustas, W. P., Nieto, H., Alfieri, J. G., Zahn, E., Gao, F., Prueger, J. H., Alsina, M. M., Hipps, L. E., McKee, L. G., McElrone, A. J., & Bambach, N. (2024). Two-source energy balance schemes exploiting land surface temperature and soil moisture for continuous vineyard water use estimation. *Irrigation Science*. https://doi.org/10.1007/s00271-024-00991-x

Padilla, A. (2024). *Almond crops and 2024 forecasted volume*. Grimm Family Center for Agricultural Business, California State University, Bakersfield. https://www.csub.edu/gfc/_files/Padilla.pdf

Parry, C. K., Nieto, H., Guillevic, P., Agam, N., Kustas, W. P., Alfieri, J., McKee, L., & McElrone, A. J. (2019). An intercomparison of radiation partitioning models in vineyard canopies. *Irrigation Science*, *37*(3), 239–252. https://doi.org/10.1007/s00271-019-00621-x

Pope, K. S., Lightle, D. M., Buchner, R. P., Niederholzer, F., Klonsky, K., Davis, U., Sumner, D. A., Stewart, D., & Gutierrez, C. A. (2016). *SAMPLE COSTS TO ESTABLISH AN ORCHARD AND PRODUCE ALMONDS*.

Priestley, C. H. B., & Taylor, R. J. (1972). On the Assessment of Surface Heat Flux and Evaporation Using Large-Scale Parameters. *Monthly Weather Review*, *100*(2), 81–92. https://doi.org/10.1175/1520-0493(1972)100<0081:OTAOSH>2.3.CO;2

Quintanilla-Albornoz, M., Miarnau, X., Pelechá, A., Casadesús, J., García-Tejera, O., & Bellvert, J. (2023). Evaluation of transpiration in different almond production systems with two-source energy balance models from UAV thermal and multispectral imagery. *Irrigation Science*. https://doi.org/10.1007/s00271-023-00888-1

Quintanilla-Albornoz, M., Miarnau, X., Pelechá, A., Nieto, H., & Bellvert, J. (2024). Assessment of upscaling methodologies for daily crop transpiration using sap flows and two-source energy balance models in almonds under different water statuses and production systems. *Hydrology and Earth System Sciences*, *28*(21), 4797–4818. https://doi.org/10.5194/hess-28-4797-2024

Rojo, F., Del Río, R., Snyder, R. L., & Zaccaria, D. (2023). A novel simulation model to predict photosynthetic active radiation interception in micro-irrigated citrus production orchards based on tree spacing, canopy geometry, and row orientation. *Computers and Electronics in Agriculture*, *212*, 108062. https://doi.org/10.1016/j.compag.2023.108062

Sánchez, J. M., Simón, L., González-Piqueras, J., Montoya, F., & López-Urrea, R. (2021). Monitoring Crop Evapotranspiration and Transpiration/Evaporation Partitioning in a Drip-Irrigated Young Almond Orchard Applying a Two-Source Surface Energy Balance Model. *Water*, *13*(15), 2073. https://doi.org/10.3390/w13152073

Sanchez, L. A., Sams, B., Alsina, M. M., Hinds, N., Klein, L. J., & Dokoozlian, N. (2017). Improving vineyard water use efficiency and yield with variable rate irrigation in California. *Advances in Animal Biosciences*, *8*(2), 574–577. https://doi.org/10.1017/S2040470017000772

Sarron, J., Malézieux, É., Sané, C., & Faye, É. (2018). Mango Yield Mapping at the Orchard Scale Based on Tree Structure and Land Cover Assessed by UAV. *Remote Sensing*, *10*(12), 1900. https://doi.org/10.3390/rs10121900

Schuepp, P. H., Leclerc, M. Y., MacPherson, J. I., & Desjardins, R. L. (1990). Footprint prediction of scalar fluxes from analytical solutions of the diffusion equation. *Boundary-Layer Meteorology*, *50*(1–4), 355–373. https://doi.org/10.1007/BF00120530

Tunca, E. (2024). Evaluating the performance of the TSEB model for sorghum evapotranspiration estimation using time series UAV imagery. *Irrigation Science*, *42*(5), 977–994. https://doi.org/10.1007/s00271-023-00887-2

Tunca, E., Köksal, E. S., Torres-Rua, A., Kustas, W. P., & Nieto, H. (2022). Estimation of bell pepper evapotranspiration using two-source energy balance model based on high-resolution thermal and visible imagery from unmanned aerial vehicles. *Journal of Applied Remote Sensing*, *16*(02). https://doi.org/10.1117/1.JRS.16.022204

Twine, T. E., Kustas, W. P., Norman, J. M., Cook, D. R., Houser, P. R., Meyers, T. P., Prueger, J. H., Starks, P. J., & Wesely, M. L. (2000). Correcting eddy-covariance flux underestimates over a grassland. *Agricultural and Forest Meteorology*, *103*(3), 279–300. https://doi.org/10.1016/s0168-1923(00)00123-4

Volk, J. M., Huntington, J., Melton, F. S., Allen, R., Anderson, M. C., Fisher, J. B., Kilic, A., Senay, G., Halverson, G., Knipper, K., Minor, B., Pearson, C., Wang, T., Yang, Y., Evett, S., French, A. N., Jasoni, R., & Kustas, W. (2023). Development of a Benchmark Eddy Flux Evapotranspiration Dataset for Evaluation of Satellite-Driven Evapotranspiration Models Over the CONUS. *Agricultural and Forest Meteorology*, *331*, 109307. https://doi.org/10.1016/j.agrformet.2023.109307

Vulova, S., Meier, F., Rocha, A. D., Quanz, J., Nouri, H., & Kleinschmit, B. (2021). Modeling urban evapotranspiration using remote sensing, flux footprints, and artificial intelligence. *Science of The Total Environment*, *786*, 147293. https://doi.org/10.1016/j.scitotenv.2021.147293

Wang, H., Jia, G., Zhang, A., & Miao, C. (2016). Assessment of Spatial Representativeness of Eddy Covariance Flux Data from Flux Tower to Regional Grid. *Remote Sensing*, *8*(9), 742. https://doi.org/10.3390/rs8090742

Wang, K., & Jin, Y. (2024). *Mapping Walnut Water Stress with High Resolution Multispectral UAV Imagery and Machine Learning* (No. arXiv:2401.01375). arXiv. https://doi.org/10.48550/arXiv.2401.01375

Wei, S., Yin, T., Dissegna, M. A., Whittle, A. J., Ow, G. L. F., Yusof, M. L. Mohd., Lauret, N., & Gastellu-Etchegorry, J.-P. (2020). An assessment study of three indirect methods for estimating leaf area density and leaf area index of individual trees. *Agricultural and Forest Meteorology*, *292–293*, 108101. https://doi.org/10.1016/j.agrformet.2020.108101

Weiss, M., Baret, F., Smith, G. J., Jonckheere, I., & Coppin, P. (2004). Review of methods for in situ leaf area index (LAI) determination. *Agricultural and Forest Meteorology*, *121*(1–2), 37–53. https://doi.org/10.1016/j.agrformet.2003.08.001

White, W. A., Alsina, M. M., Nieto, H., McKee, L. G., Gao, F., & Kustas, W. P. (2019). Determining a robust indirect measurement of leaf area index in California vineyards for validating remote sensing-based retrievals. *Irrigation Science*, *37*(3), 269–280. https://doi.org/10.1007/s00271-018-0614-8

Wu, J., Chen, P., Fu, S., Chen, Q., & Pan, X. (2023). Co-inversion of island leaf area index combination morphological and spectral parameters based on UAV multi-source remote sensing data. *Ecological Informatics*, *77*, 102190. https://doi.org/10.1016/j.ecoinf.2023.102190

Wu, S., Deng, L., Guo, L., & Wu, Y. (2022). Wheat leaf area index prediction using data fusion based on high-resolution unmanned aerial vehicle imagery. *Plant Methods*, *18*(1), 68. https://doi.org/10.1186/s13007-022-00899-7

Xia, J., Ning, L., Wang, Q., Chen, J., Wan, L., & Hong, S. (2017). Vulnerability of and risk to water resources in arid and semi-arid regions of West China under a scenario of climate change. *Climatic Change*, *144*(3), 549–563. https://doi.org/10.1007/s10584-016-1709-y

Xiang, W., Rong, X., Yan, W., Qi, X., Wang, H., Jin, S., & Ai, J. (2022). Spatial Representativeness of Eddy Covariance Measurements in a Coniferous Plantation Mixed with Cropland in Southeastern China. *Remote Sensing*, *14*(19), 5022. https://doi.org/10.3390/rs14195022

Xu, K., Sühring, M., Metzger, S., Durden, D., & Desai, A. R. (2020). Can Data Mining Help Eddy Covariance See the Landscape? A Large-Eddy Simulation Study. *Boundary-Layer Meteorology*, *176*(1), 85–103. https://doi.org/10.1007/s10546-020-00513-0

Yan, G., Hu, R., Luo, J., Weiss, M., Jiang, H., Mu, X., Xie, D., & Zhang, W. (2019). Review of indirect optical measurements of leaf area index: Recent advances, challenges, and perspectives. *Agricultural and Forest Meteorology*, *265*, 390–411. https://doi.org/10.1016/j.agrformet.2018.11.033

Yi, C. (2008). Momentum Transfer within Canopies. *Journal of Applied Meteorology and Climatology*, *47*(1), 262–275. https://doi.org/10.1175/2007JAMC1667.1

Zarate-Valdez, J. L., Whiting, M. L., Lampinen, B. D., Metcalf, S., Ustin, S. L., & Brown, P. H. (2012). Prediction of leaf area index in almonds by vegetation indexes. *Computers and Electronics in Agriculture*, *85*, 24–32. https://doi.org/10.1016/j.compag.2012.03.009

Zhang, C., Valente, J., Kooistra, L., Guo, L., & Wang, W. (2019). OPPORTUNITIES OF UAVS IN ORCHARD MANAGEMENT. *The International Archives of the Photogrammetry, Remote Sensing and Spatial Information Sciences*, *XLII-2/W13*, 673–680. https://doi.org/10.5194/isprs-archives-XLII-2-W13-673-2019

Appendix A sUAS Flights

Table 1 sUAS flights executed during IOPs in 2021 and 2022 by AggieAir, with multispectral and thermal imagery information.

Day	Date	Local Time	Location	Payload	Bands	Resolution (cm)
1	07/29/2021	15:10	OLA	AggieAir sensor	RGB, NIR, TIR	9.2 / TIR 58.1
2	08/05/2021	11:30 / 13:05 / 15:30	OLA	AggieAir sensor	RGB, NIR, TIR	9.1 / TIR 55.8
3	07/07/2022	11:24 / 12:49 / 15:12	OLA	MS Altum PT	RGB, RedEdge, NIR, TIR	22.0 / TIR 22.0
4	07/08/2022	11:19 / 12:52 / 15:14	OLA	MS Altum PT	RGB, RedEdge, NIR, TIR	22.2 / TIR 22.2
5	07/10/2022	11:37 / 12:50 / 15:15	WWF	MS Altum PT	RGB, RedEdge, NIR, TIR	5.3 / TIR 5.3
6	07/14/2022	11:35 / 12:49 / 15:21	WWF	MS Altum PT	RGB, RedEdge, NIR, TIR	5.3 / TIR 5.3
7	09/08/2022	11:29 / 12:44 / 15:14	VAC	MS Altum PT	RGB, RedEdge, NIR, TIR	5.5 / TIR 5.5
8	09/09/2022	11:29 / 12:44 / 15:14	WWF	MS Altum PT	RGB, RedEdge, NIR, TIR	5.5 / TIR 5.5

MicaSense (now: AgEagle Aerial Systems Inc., https://ageagle.com/)

Appendix B Infrared Thermometer (IRT) Correction Equation

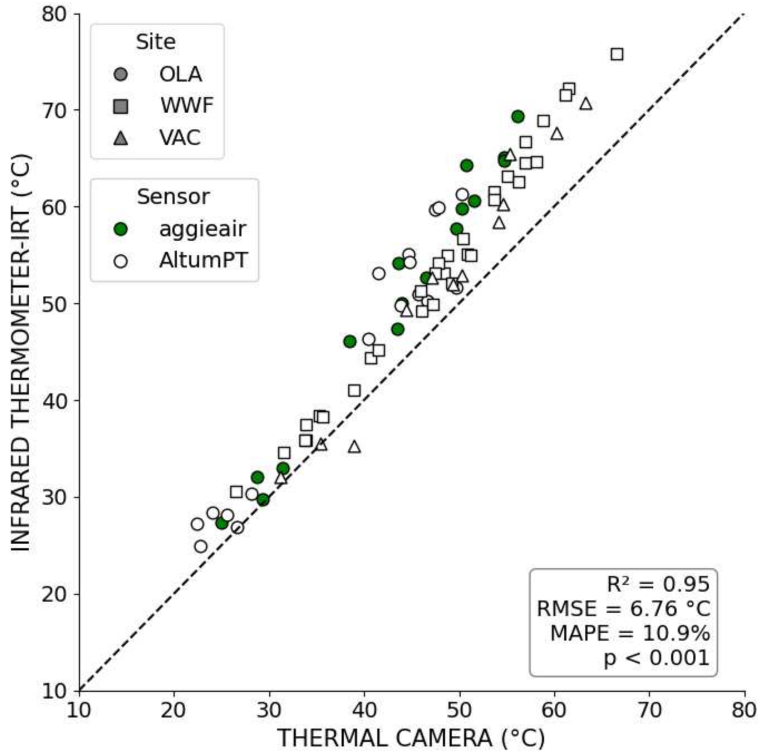

Figure 11. General thermal correction equation with IRTs measurements (observed values) for different thermal cameras, measurements done throughout 2021-2022 IOPs, at the three different sites (OLA, WWF, and VAC).

Appendix C Proposed LAI Model Pseudo-Code

Algorithm 1: LAI Estimation from sUAS Imagery

Input: Multispectral sUAS imagery (Red and NIR bands); canopy-NDVI pixel thresholds

Output: Leaf Area Index (LAI) map

Step 1: Preprocessing

Georeference and orthorectify the imagery.
Apply radiometric corrections to the raw sUAS imagery.

Step 2: NDVI Calculation

For each pixel, compute NDVI as:

NDVI = (NIR - Red) / (NIR + Red)

Step 3: Canopy Masking

Generate a binary canopy mask using an NDVI threshold.

Step 4: NDVI Aggregation at Tree Scale

For each grid cell (6.5 m):

- Apply the NDVI mask to extract canopy NDVI values
- Assign a value of zero to non-canopy areas
- Compute the average NDVI within each grid cell

Step 5: FC Calculation

For each grid cell (6.5 m):

Calculate the canopy fractional cover (FC) based on the NDVI mask.

Step 6: LAI Estimation

For each grid cell:

Estimate LAI using the empirical model:
LAI = (NDVI + b) / (FC + c)
Where b and c are empirically determined constants.

Step 7: Output

Export the resulting LAI map as a raster file.